

Developing detector technologies to map the diffuse Universe: Characterizing the dark current plateau in silicon detectors with EMCCDs

**Aafaque R Khan^{a,*}, Erika Hamden^a, Gillian Kyne^b, April Jewell^b, Todd Jones^b,
Vincent Picouet^b, Harrison Bradley^a, Ipek Kerkesser^a, Todd Jones^b, Brock Parker^a,
David Beaty^a, Frank Gacon^a, Jhon Ford^a, Grant West^a, Paul Arbo^a**

^aThe University of Arizona, Hamden UV/Vis Detector lab, Steward Observatory, 933 N Cherry Avenue,
Tucson, Arizona, United States of America, 85721

^bJet Propulsion Laboratory, 4800 Oak Grove Dr, Pasadena, California, United States of America, 91011

Abstract. Recent technological advancements in processing Silicon-based detectors like delta doping and Atomic Layer Deposition (ALD) anti-reflection (AR) coatings, developed by the Microdevices Laboratory (MDL) at the Jet Propulsion Lab (JPL), have unleashed a new class of high Quantum Efficiency (QE) Ultraviolet detectors. Combined with improvements in the performance of UV reflective coatings, these detectors have enabled a proliferation of UV missions (like FIREBall-2, SPARCS, SHIELDS) and proposals/concepts (like Hyperion, UVEX,, Nox, Eos, among others). The growing profile of these detectors drives the need to understand and optimize their noise performance. In this paper, we provide an overview of our detector noise characterization test bench that uses delta-doped, photon counting, Electron-multiplying CCDs (EMCCDs) to understand the fundamental noise properties relevant in all Silicon CCDs and CMOS arrays. The focus of our current work is to identify the source of dark current plateau, a noise floor that limits the Signal-to-Noise Ratio (SNR), and overall performance that can be achieved with photon-counting detectors. While it is expected that the thermal dark current in silicon detectors should decrease exponentially with temperature, previous dark measurements with EMCCDs have shown to plateau below a temperature of -110°C. It is suspected that this plateau could be due to a combination of detectable photons in the tail of blackbody radiation of the ambient instrument, low-level light leaks, and a non-temperature-dependent component that varies with substrate voltage. To further investigate this dark plateau, we developed an innovative test setup to control the temperature of the detector and its ambient environment independently. To achieve this the detector is surrounded by a thermal shroud that is cooled by a liquid nitrogen cooling chain while the detector is cooled by an independent cryocooler cooling chain. We measured the dark current with different combinations of the detector (between -85 °C to -130°C) and shroud temperatures (25 °C to -85 °C) and detector substrate voltages (VSS). For these measurements, we used delta-doped Te2v 201-20 EMCCDs provided by MDL readout with a Nüvi CCCP v3 controller at 1 MHz. **We found the dark current plateau below -100 C when detector is operated without a cold shroud but with the shroud cooled to 230 K ... [Add description of the results]**

Keywords: EMCCD, dark current, UV Astronomy, photon counting, delta-doped CCD, dark current plateau, Detector characterization.

*Aafaque R Khan, arkhan@email.arizona.edu

1 Introduction

Silicon-based Ultraviolet (UV) detector technology has made a giant leap in the last two decades. Detectors processed with delta-doping,¹⁻³ a Molecular Beam Epitaxy (MBE) process developed at the Micro-Devices Laboratory (MDL) at the Jet Propulsion Lab (JPL), have been demonstrated to achieve Internal Quantum Efficiency (IQE) of up-to 100% in the UV/Optical spectrum.⁴⁻⁶ Combined with Atomic Layer Deposition (ALD) anti-reflection (AR) coatings these devices reach up to 60% Quantum Efficiency (QE) in the UV.⁶⁻⁸ This new class of high-QE Ultraviolet detectors has led to a proliferation of sub-orbital and orbital UV missions (e.g. FIREBall-2,⁹ SPARCS¹⁰) and concepts (like Hyperion,¹¹ Nox,¹² Eos,¹³ among others). The growing profile of these detectors drives the need to understand and optimize their noise performance.

Electron-Multiplying Coupled Devices (EMCCDs)^{14,15} have emerged as an exciting detector option in astrophysics due to their photon-counting capability and low read noise ($\ll 1\text{e-}/\text{pixel/frame}$)^{5,16}. These detectors are specifically favorable for photon-starved UV astronomy where the low background (an order of magnitude lower than visible) allows high-sensitivity measurements that are typically limited by the detector noise and instrument background. The first sub-orbital demonstration of a UV-enhanced, delta-doped, ALD-coated EMCCD detector was flown on the Faint Intergalactic Red-shifted Emission Balloon (FIREBall-2, hereafter FB2) in 2018.⁹ Similar devices that are optimized for

Optical/Near-Infrared will fly on the Coronagraphic Instrument (CGI) of the Nancy Grace Roman Space Telescope.¹⁷

The single photon counting capability of EMCCDs makes them an excellent tool for the precision measurement of noise characteristics of similar Silicon CCD and CMOS arrays. The EMCCD architecture overcomes the low-frequency readout noise, the limiting noise in conventional CCDs, by amplifying the signal in the serial gain registers using avalanche multiplication.¹⁸ EMCCDs can accommodate a wide dynamic range of signals by operating with a variable gain (from $>1,000$ e⁻/e⁻ in photon-counting mode to 1 for conventional CCD mode.¹⁹ But with this pre-amplifier gain approach, the noise due to dark current and Clock Induced Charge (CIC), which is normally negligible compared to read noise in traditional CCDs, is also amplified like the photo-electrons. Furthermore, the avalanche multiplication process generates additional noise from cosmic ray trails, deferred charge, and coincidences.^{19,20}

Previous efforts to optimize the noise performance of these devices including improving the readout electronics,^{21–23} detector cooling, innovative clock shaping,^{5,22,24} and modifications to the device architecture¹⁷ have resulted in a significant reduction in the noise floor. The CIC and dark current remain the noise-limiting factor in the performance of these devices. The dark current in silicon devices is expected to decrease exponentially with detector temperature. However, previous measurements with EMCCDs have shown

it to plateau around a detector temperature of 163 K (see section 2.2). This plateau is responsible for a noise floor that limits the signal-to-noise ratio (SNR) and overall performance that can be achieved with these detectors.

In this paper, we report the design of a novel test setup to further investigate the dark plateau using delta-doped Te2v 201-20 EMCCDs provided by MDL combined with a Nüvü CCCP v3 controller. The setup allows control of the temperature of the detector and its ambient environment independently. We present our first measurements of dark current with different combinations of the detector and ambient temperature and detector substrate voltages (VSS).

2 Motivation

2.1 Advancing UV detectors for new perspectives on galaxy evolution

Mapping the distribution and flow of baryons at different scales of the universe is necessary to understand the formation and evolution of galaxies and stars.²⁵ A significant fraction of baryons in the universe reside outside of galaxies and are difficult to observe and account for.^{26–28} Recent simulations and observations to resolve the ‘missing baryon’ problem point to three possibilities: the baryons could be distributed in larger-scale filamentary structures in the cosmic web,^{29,30} in clouds of warm gas in galactic halos,^{31,32} or in a dilute hydrostatic halo of hot gas near the virial temperature.^{33–35}

Extensive Ultraviolet (UV) observations are required to probe the density, morphology, physical extent and kinematics of this tenuous gas in the Intergalactic (the cosmic web), and Circumgalactic (warm and hot gas around galaxies) matter (IGM, and CGM, respectively).^{25,36} UV observations offer a cornucopia of spectral features (absorption/emission lines, continuum emission, and fluorescence) from atomic and molecular hydrogen (for e.g., Ly- α from HI) and trace metals (for e.g., OIV, CIV, NV, MgII, etc.) that can be used to study these media.^{37,38} While these emission signatures are typically very faint, deep observations are possible due to the very low UV sky background which is several orders of magnitude below that of the visible.³⁶ The challenge for galaxy evolution studies, then, is to detect the faint UV signals that are expected from this mostly unobserved diffuse gas in galactic halos.

Despite the scientific value of UV observations of emission from the faint IGM and CGM, there are precious few telescopes currently carrying out these observations (e.g. Hubble Space Telescope-Cosmic Origins Spectrograph, HST/COS³⁹). This is partly due to historical limitations of UV detectors and mirror technology including low efficiencies, low reflectivity, and impact of contamination. A concerted effort by the UV community over the last decade, supported by the Decadal⁴⁰ and NASA priorities,⁴¹ have resulted in more advanced detectors and mirror coatings.^{4,42} These high-efficiency UV detectors and stable, high-reflectivity coatings are motivating an explosive growth in the number of UV

mission proposals.

2.2 Dark current Plateau

In previous measurements for the FB-2 flight detectors (the Te2V EMCCD 201-20), Kyne et al.^{5,20} found that the CIC can be reduced with lower parallel and serial wells as well as optimizing the clock shaping. After achieving optimal CIC, they also investigated the variation of dark current with detector temperature and substrate voltages. It was found that the dark current decreased with detector temperature as expected until plateauing at \sim 163 K. Lowering the temperature beyond this did not significantly reduce the Dark Current (Figure 1).

It is suspected that this plateau could be due to a combination of ambient VIS/IR from the Dewar, low-level light leaks, and/or a non-temperature dependent component, that varies with substrate voltage, caused by spurious charge generation in the detector pixels and/or emission from the detector packaging. Similar plateaus have been observed in other CCDs and an investigation to understand this noise will have a wide and profound impact on understanding low-noise CCDs and CMOS arrays of all types.

We hypothesize that the dark plateau measured in the EMCCDs is not caused by the intrinsic thermal dark current in the pixels and is from the visible photons in the tail of thermal black-body emission from the surrounding hardware. Unlike infrared telescopes and instruments, where both the detectors and the telescope structures are cooled, UV

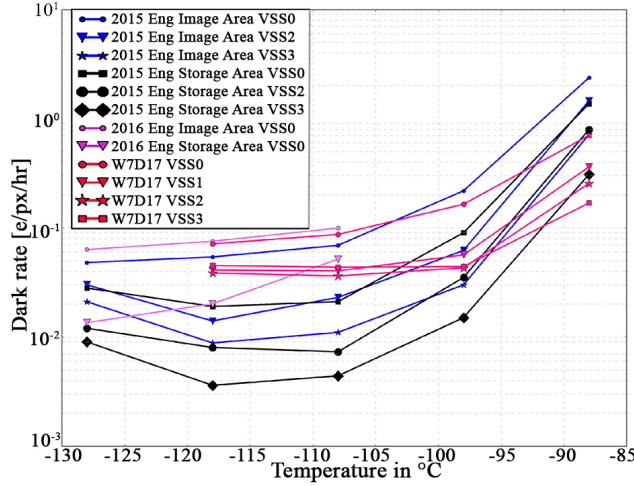


Fig 1: Dark current rates as a function of temperature. This plot shows dark current rates for two engineering-grade devices and a delta-doped device with a 10 MHz serial clock. The image area and storage area are plotted for engineering devices. Colors represent different devices and substrate voltages. (Adapted from Kyne 2016⁵)

and optical instruments do not employ cooling of the mechanical surrounding structure of the telescope and camera. To test this hypothesis, we employ two independent cooling chains to cool the detector and the surrounding environment and measure the dark current at different combinations of temperatures and substrate voltages.

3 Design of the EMCCD Dark characterization setup

To test our hypothesis, we developed a novel detector characterization test setup that allows us to control the detector and the surrounding temperature independently. The thermal control system has been designed with control authority to operate the detector at any temperature between 140 K to 180 K, while the shroud can be kept at any temperature between room temperature to 170 K. The schematic of the dark characterization test setup

is shown in Figure 2. The detector and front-end electronics are housed in a high vacuum enclosure consisting of an ND8 dewar from IRlabs and a custom-built extension. The vacuum enclosure is evacuated by a TPS-flexi vacuum pumping system from Agilent. The detector is connected to the cold tip of a Cryotel MT Cryocooler. The cryocooler is controlled by a closed-loop controller that monitors a Pt-100 temperature sensor on the cold tip to maintain it at a fixed programmable temperature. A Lakeshore Model 350 controller provides the precision temperature control of the detector with patch heaters and temperature sensors mounted in proximity to the detector. The detector is surrounded by a shroud that is connected to the LN2 cold plate of the Dewar. For cooling the shroud, the Dewar is filled with LN2 and the Lakeshore controller uses Pt-100 sensor and patch heaters on the shroud to control its temperature. The LN2 level in the Dewar is maintained by a Norhof automated LN2 micro-dosing system to allow multi-day operations without a manual LN2 refill. In the following sections, we describe the design of different subsystems of the test setups.

3.1 Vacuum system

The detector and Front-End Electronics (FEE) Printed Circuit board (PCB) are housed in a vacuum enclosure that consists of an ND-8 Dewar from IR-Labs with a custom-designed stainless steel extension shown in Figure 3. The FEE PCB is mounted on three stand-offs that minimize the heat leak from the board to the mechanical mounts. These standoffs are

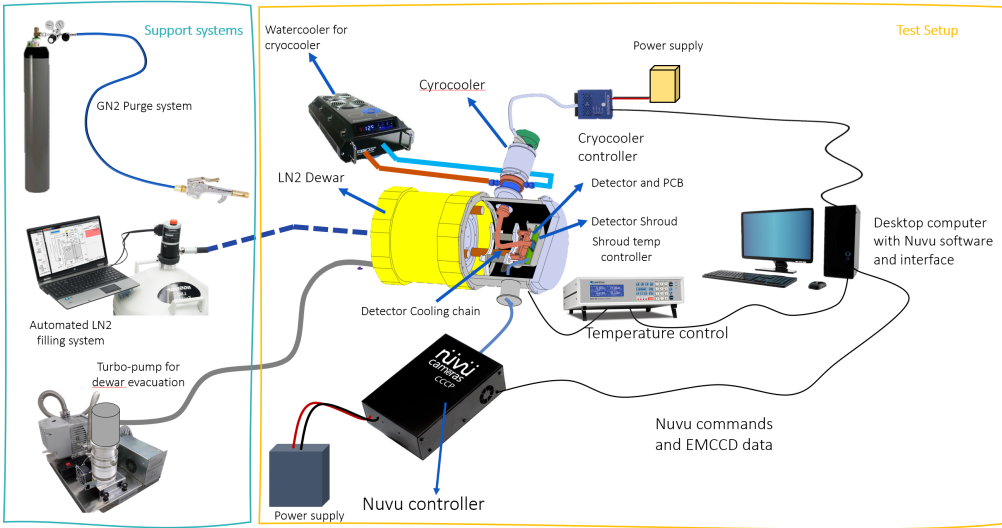


Fig 2: Schematic of the test setup, illustrating the vacuum Dewar, detector and detector controller, detector and shroud cooling systems, and ancillary components including the water cooling for the cryocooler, vacuum pump system, automatic LN₂ refill system, and Ultra-High Purity Gaseous Nitrogen supply for purging. [Draft Figure]

supported by an interface ring (Al 6061-T6) that also provides mechanical support for the cold finger assembly. The interface between the cold finger assembly and the ring consists of two Titanium alloy (6Al-4V) supports that minimize thermal conductivity between the cold finger and the adapter ring. These spacers also act as a metering structure due to their low thermal expansion coefficient. The cold finger assembly is connected to the Cryocooler by a flexible copper strap. The adapter ring is mechanically supported by three high-density Teflon posts that are attached to the spider adapter. The spider adapter has three extensions that mount onto the external shroud. The multiple levels of insulation in this mounting scheme minimize the parasitic heat load to the detector at cryogenic temperatures from the body of the vacuum enclosure at room temperature.

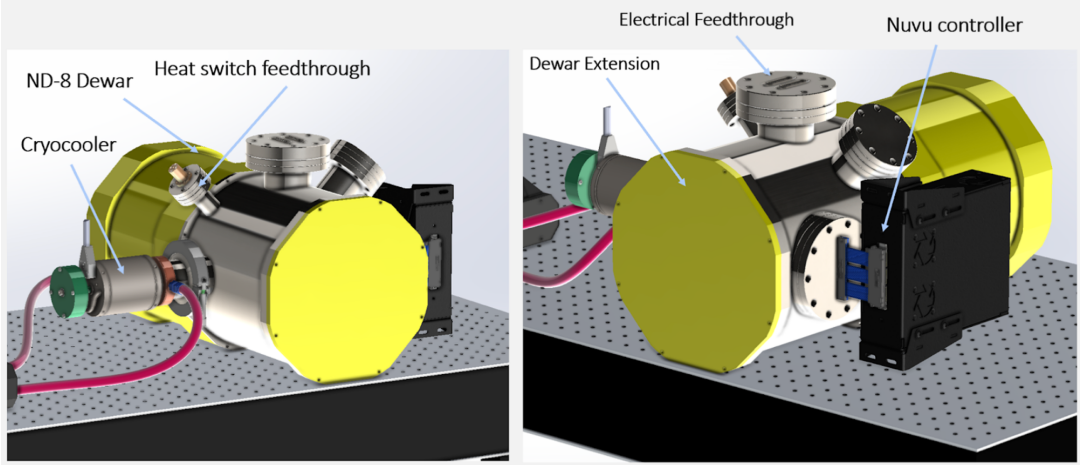


Fig 3: Custom Vacuum Dewar setup. CAD representations of vacuum setup depicting the custom extension attached to the ND8 Dewar and the configuration of the cyrocooler, Nüvü CCCP v3 controller, interfaces for the mechanical heat-switch and electrical feed-throughs.

The extension has vacuum interfaces for electrical feed-through for temperature sensors and heaters, a custom electrical feed-through for Samtech High-Speed Coaxial cable assembly that connects the detector front-end board in vacuum to the detector controller, an interface flange for the cold-tip of the cryocooler, and a custom flange for a manual actuator for a mechanical heat switch that controls the thermal conductivity between the thermal shroud and the cold surface of the LN₂ Dewar. The Dewar and extension are pumped to around 10^{-6} mbar by a combination of a dry-scroll and turbo-molecular pump.

3.2 Detector Cooling-chain

Figure 4 shows CAD view of the detector cooling-chain. The cold finger assembly consists of two gold-plated copper cold fingers. Cold finger 1 (CF1) is in direct contact with the

back of the detector and is thermally connected to Cold Finger 2 (CF2) with two small flexible copper straps. The CF1 is connected to the cold tip of the cryocooler with a long flexible copper strap. Indium foils are used at all thermal interfaces to improve contact conductance. The mechanical connection between the two cold fingers is through four Invar spacers that act as thermal insulators and metering structures. The motivation for this unique design was to minimize the stress on detector package that are present in detector mounting schemes that use a clamping force. In addition, this design allows for easier installation and replacement of detectors on the ZIF socket.

This design has been optimized such that the back of the detector and the tip of CF1 have no differential thermal expansion when the detector is cooled from room temperature to at least -130 °C at a controlled cooling rate. We used Finite-Element Modeling (FEM) to perform a coupled thermo-elastic deformation study to estimate the steady-state temperatures and resultant thermo-elastic deformation of the assembly. Using boundary conditions for the lowest expected operational temperature of the cryocooler and detector, we found that the worst-case relative deformation between the tip of the cold finger and the detector back was expected to be <40 microns. We found that the resultant displacement would increase the contact pressure of the detector and cold finger interface thus slightly improving the thermal conductivity. Based on this steady-state study, we decided to build and test the performance of the system for transient performance and dynamic loading

during cooling and switchover between different detector temperatures. During testing, we found that the cold finger scheme works as designed but the cooling rate should be limited to maintain the difference between the CF1 and CF2 temperatures to within 4 K. If the temperature difference exceeds this value the detector and the tip of CF1 lose contact. The interface acts like a thermostat and prevents the detector from cooling down.

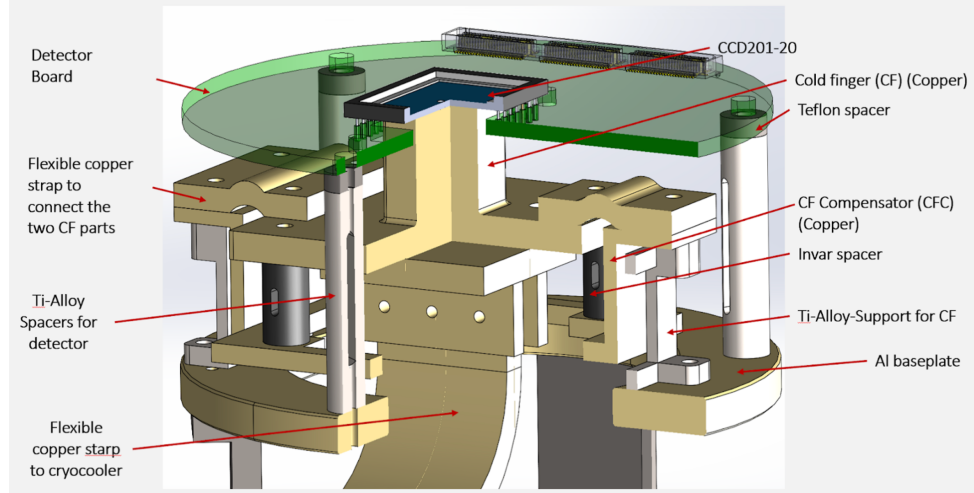


Fig 4: Detector Cold finger design. CAD view showing the two part copper cold finger. The cold finger 1 (CF1 and cold finger 2 (CF2) are designed to maintain the contact between the back of the detector and the tip of the CF1 from room to cryogenic temperature. An Invar spacer is between the CF1 and CF2 acts like a metering structure while the thermal contact between the two is through two flexible copper straps.

3.3 Thermal Shroud Cooling chain

The schematic for the thermal cooling shroud is shown in Figure 5. The challenge with this design was to insulate this cooling chain, except the minimal radiation coupling, from the detector cooling chain. To address this channel the shroud was designed ensure

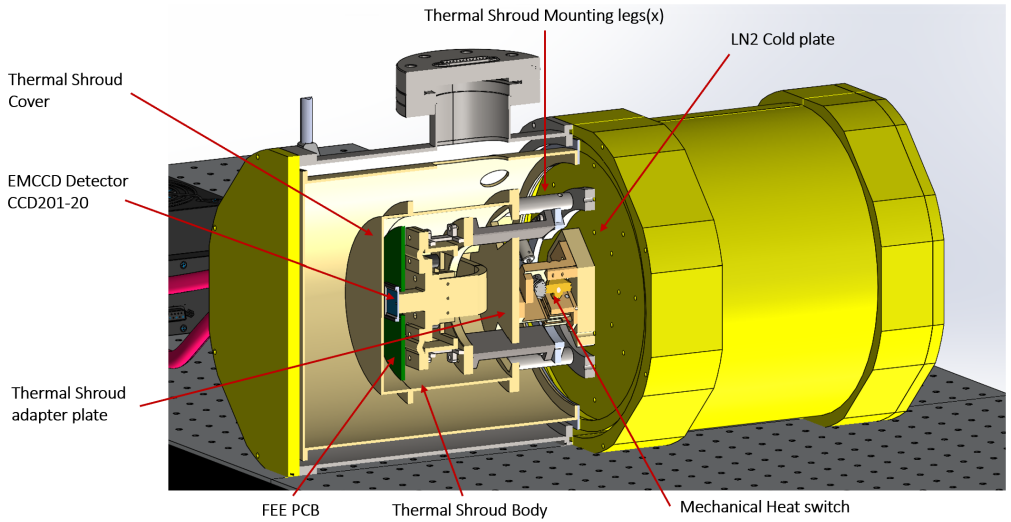


Fig 5: CAD section of the thermal shroud cooling chain. The shroud surrounding the detector and FEE is cooled through a direct conductive path to the LN2 vessel. A temperature sensor on the shroud is used to control the temperature with patch heaters operated by a closed-loop temperature controller.

that any direct line of sight from the detector points to the thermal shroud. Additionally, the shroud also blocks indirect light-leak paths from the warm surfaces of the vacuum enclosure, that can reach the detector. The thermal shroud is mounted on an aluminum cold plate that is mechanically supported on the LN2 cold interface. The thermal contact between the LN2 cold interface and the aluminum cold plate is through a mechanical heat switch from IR-Labs. The mechanical heat switch can be actuated from outside the chamber with a plunger that goes through a vacuum feed-through. This interface allows us to vary the thermal conductivity of the link between the LN2 cold interface with the shroud assembly. The Lakeshore temperature controller provides closed-loop temperature control using temperature sensors and patch heaters mounted on the shroud.

4 Detector and detector controller

The dark measurements are performed with custom back-thinned EMCCDs from Teledyne-e2v (Te2v, Chelmsford, UK). It is **an engineering-grade Te2v CCD 201-20 model** processed and packaged by the Micro-devices Laboratory (MDL) at the Jet Propulsion Laboratory (JPL Pasadena, California, USA). The commercial versions of this model are designed to operate in frame transfer mode, with a 1kx1k image area and a 1kx1k transfer area. However, our detectors were customized to operate in the line transfer mode to read the full 2kx1k frame. Unlike commercial devices, the storage area of our detectors does not have a shield. This modification allows us to use the storage area pixels for imaging and is desired for applications such as wide-field multi-object spectroscopy.⁹

The detectors are delta-doped with Molecular Beam Epitaxy (MBE) followed by custom UV anti-reflection coatings deposited using Atomic Layer deposition (ALD). Both these processes are done at the wafer level, after which back-thinning, dicing, and packaging are performed to make individual detectors. Similar processing was performed on devices used in previous work on the study of dark current characteristics of EMCCDs for FB2.⁴³

We use the CCCP v3 controller from Nüvü Camēras for detector readout. These controllers provide parametric control of the bias levels, clock shapes, timings, and amplitudes to develop custom readout sequences.¹⁹ This allows us to develop and test different readout sequences to optimize the noise performance. For instance, changing the amplitude

and shape of the phase clocks to minimize the noise due to Clock Induced Charge (CIC).

The controller has two outputs, one with 1 or 2 MHz and the other with 10 or 20MHz, high-voltage serial clocks. For this work, the FEE is configured for the 1 MHz clock.

The FEE PCB design is derived from the design of FB2 flight boards. We audited the original design and made several modifications to improve the noise performance of the boards. These include increasing the number of layers to separate tracks for bias and the clock lines, adding grounding planes between the layers, optimizing the track widths and net layout for better isolation, and replacing components with lower noise counterparts. We also added a grid of vias to connect all ground planes to improve the grounding. We also replaced the SIP (Single In-line Package) receiving sockets for the detector with a Zero Insertion Force (ZIF) Socket. The ZIF socket allows faster and more convenient replacement of the detectors for our test setup. We customized a 3M 17x17 pin ZIF socket (PN:200-6317-9UN-1900) by disassembling the package and creating a cutout through the socket for the cold finger. The gold-coated beryllium copper pins were populated based on the detector footprint and the ZIF socket was soldered onto the board. As the physical footprint of the ZIF socket is larger than the SIP sockets, we reorganized the tracks on the board and also moved the signal conditioning components to the back face of the board. The Nüvü controller has two different high voltage clock outputs but only one of them can be used at a time. The original design for the boards had a switch selector to select which

HV clock output from the controller is connected to the HV clock pin on the detector. We replaced this component with trace cuts for our lab boards and used a zero Ohm resistor to select the track connecting to the detector HV pin. While it is possible to swap the resistor from one track to the other on the same board, we decided to make two different versions of the board for the 1 MHz and 10 MHz HV clocks. This work uses the 1 MHz board.

All these improvements lead to a factor of five reduction in the read noise compared to the original boards. This is significant as the detective quantum efficiency of EMCDDs operated in PC mode depends on the ability to discriminate the pixels with the signal from the pixels with read noise (σ). This is achieved by selecting a multiplication gain (G) such that $G/\sigma > 50$ ensuring that $\sim 90\%$ of events are counted when a 5σ cut-off is used for PC threshold.⁴⁴

5 Control and Acquisition Software

We used automated data acquisition software to remotely operate the detector controller and ancillary support systems including the Cryocooler controller, Lakeshore temperature controller, and Liquid Nitrogen (LN2) control system. The end-to-end acquisition is executed through a Python app that can be configured to run exposure sequences with different values of controller parameters, detector, and shroud temperature settings.

For image acquisition with the Nüvü CCCP controller,⁴⁵ the Python app sends shell commands to a back-end server application. The code for the back-end server and the

scripts for the python app were adopted from Kyne et. al. **citation needed**. The back-end executable application, written in C using the API guidelines provided by the Nüvü Camēras, directly handles the acquisition of images with controller settings (exposure time, shutter control, EMgain, etc.) and saves individual or bursts of images as FITS files. The Python scripts work synchronously with the back-end server to perform operations like file handling, configuring parameters for the image sequences, acquiring and storing metadata, waiting for the back-end server, and saving the run-time log and database at the end of acquisition. During acquisition, Quick-look images are displayed in SAO DS9 using pyds9 python package that communicates with DS9 via the XPA messaging system.⁴⁶

The readout sequence for the detector was programmed directly on the FPGA flash memory of the CCCP controller using the CCCP Comm application provided by Nüvü Camēras. During acquisition, the back-end server can be commanded to select any readout sequence written to the controller’s flash memory. We adopted a readout sequence developed for FB2 flight detectors and optimized it for our laboratory detector, new boards, and signal chain. This work’s readout sequence optimization process is discussed in section 6.3.

The ancillary systems are operated through standalone Python servers that communicate to the controllers via serial commands. The temperature server acquires temperature sensor data from the Lakeshore temperature controller for the sensors on the detector,

thermal shroud, and the two cold-fingers, and the Cryocooler controller for the sensor on the cryocooler cold tip. The temperatures are logged and displayed on an interactive real-time web server. An independent server controls and monitors the turbo pump via the pump controller and logs the pressure of the Dewar. The automated LN2 dispenser is programmed using Windows-based GUI software provided by the manufacturer on a separate machine. The automation commands and scripts were bench-tested in trial runs by manually reviewing and verifying the acquisition logs and output files.⁴⁵

6 Implementation, optimization and testing

Figure 6 shows the flow of the end-to-end test plan for the dark characterization. Before the dark current measurements, we conducted robust testing and characterization of the signal chain and the cooling system to ensure that live detectors would not be damaged during operations. Furthermore, the noise and performance characteristics of these detectors such as Charge Transfer Efficiency (CTE) and multiplication gain are sensitive to temperature. Therefore, it was important to ensure that there were no unwarranted temperature fluctuations and drifts. We tested the functionality and performance of the new FEE PCB with the Nüvü controller before connecting a live detector. The detector cooling chain was tested and calibrated using a mechanical detector with a temperature sensor on the active area. We also tested the thermal shroud cooling chain and calibrated the control loop at different shroud temperatures.

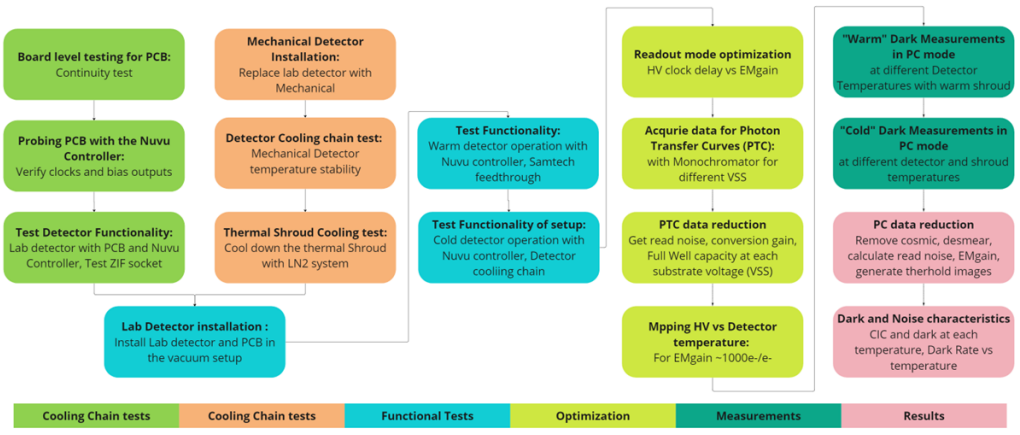


Fig 6: Test flow diagram shows all the tests and validation steps involved in the characterization of the detector CIC and dark noise.

6.1 PCB and signal-chain validation

The populated PCBs were first tested at board level for continuity and then connected to the Nüvü controller without a detector. Each pin on the ZIF socket was probed using a Tektronix Mixed Signal Oscilloscope (MSO2024B) while the controller was configured to run a readout sequence with High voltage clock enabled. We verified the functionality of the boards by comparing the measured values of voltages for all bias outputs and the amplitude, shape, frequency, and delays for the parallel, serial HV clock outputs with the expected values programmed in readout sequences. We also compared the results with the measurements on a board fabricated from the original layout. Based on this initial testing, we reassigned some bias addresses in the controller to match the readout sequence. Figure 7 (Panels b-d) shows the measured waveforms for the HV, phase, and serial clocks probed on pins of the ZIF socket of the 1 MHz board. Further validation and optimization of

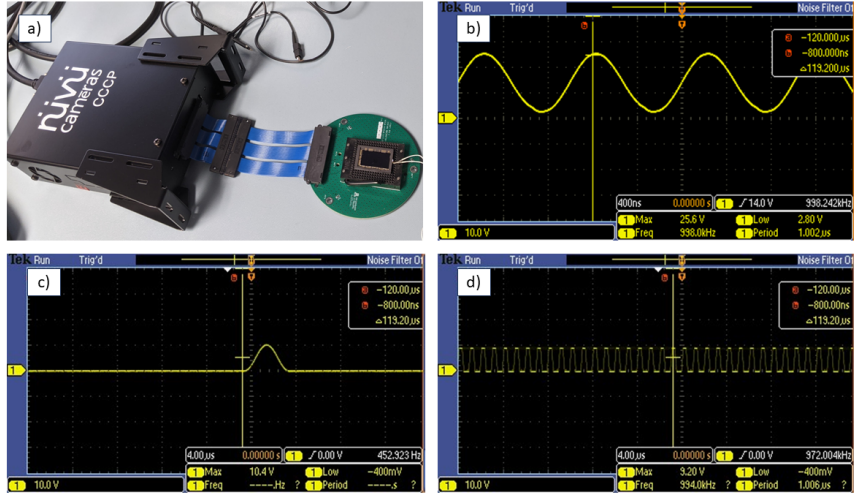


Fig 7: PCB validation testing: a) Bench test setup for Laboratory detector with the 1 MHz board with the Nüvü controller. Waveforms for High voltage clock (b), one of the four phases of Image clock (c), and one of the serial clocks (d) are shown. These were measured by probing the corresponding pins on the ZIF socket of the 1 MHz board. The HV and the image clocks have a sinusoidal profile while the serial clocks have arbitrary shapes.

the boards and readout sequences were done using a live detector during warm and cold operations.

6.2 Functional test of cooling chains

To test the detector cooling chain and calibrate the detector temperature, we used a non-functional detector with a Pt-100 Platinum RTD directly bonded to the imaging array with suitable epoxy. We conducted several cooling runs with different operation configurations for Cyrocooler and parameters for heater closed-loop control for the Lakeshore controller. The temperatures for the detector sensor and the two cold fingers were simultaneously monitored and logged during each run. After a few iterations, we fixed suitable

PID parameters for the CF2 heater channel and a sequence for the cryocooler and heater operations. The cryocooler had to be operated intermittently to minimize the cooldown time for the detector while maintaining the cooling rate constraints for the detector and the athermalized cold finger design. We observed that there was no long-term temperature drift even if the setup was operated for several days and the detector temperature was maintained to better than +/- 0.3 K. Panel b in Figure 8 shows the mechanical package of the detector with the temperature sensors bonded to the image area. We tested the cooling scheme with our laboratory detector and the sample of the typical temperature profiles of the detector and cold finger temperatures is shown in Figure 9. The laboratory detector has a temperature sensor on the package. The offset between the temperature between the sensor calculated by comparing the cooling tests results for the two detectors. We have swapped detectors from this cooling setup several times and have repeatably achieved the same performance during several cooling cycles.

6.3 Optimization of Readout Sequence

After the board level validation and the cooling test for the detector cooling chain, we mounted the live detector on the board to test the readout sequence. The readout sequence is specific to a detector and board combination and is sensitive to the detector temperature. We optimized the readout sequence for the new detector and board combination and characterized the temperature dependence for each detector operational temperature. We

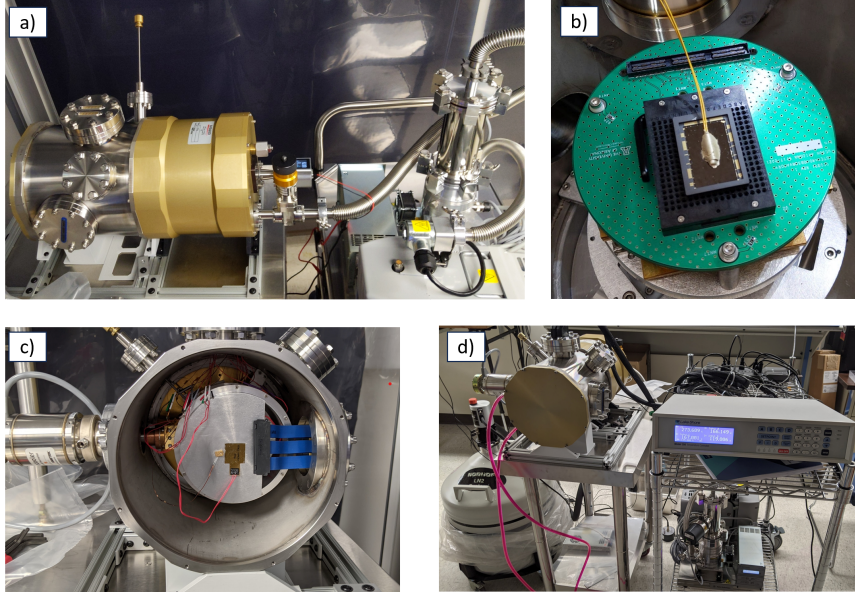


Fig 8: Images showing the different components of the test setup. a) Vacuum Dewar with the turbo pump The custom Samtech flange and the flange for thermal sensor and heater wiring, b) Mechanical detector package with the temperature sensor bonded on the surface of the sensor, c) Internal view of the Dewar showing the vacuum shroud and the Samtech cable. d) Experimental setup, consisting of Dewar, detector controller, the LN2 cooling system, temperature controller, and vacuum pump.

adopted the clock amplitudes, shapes, and timings from the FB2 readout sequence that were designed and tested to minimize the parallel and serial CIC.⁴³ We programmed the controller with sequences and acquired images using the GUI applications provided by Nüvü Camēras . The software suite consists of CCCP server app to establish connection to the camera firmware, CCCP Comm app to create and program the customized readout sequences and change clock and bias values, and CCCP View app for image acquisition and diagnostics. As expected, without changes to the sequence we got a garbled image that was corrected by adjusting the High Voltage clock delay time to recover a sharp im-



Fig 9: Sample of the temperature profile for cooling the detector. The cryocooler is intermittently shut to keep the CF1 in contact with the detector back-plane and to keep the detector cooling rate of the detector well within 5K/min limit.

age boundary between the prescan, image, and overscan regions. This delay adjustment synchronizes the HV register with the serial register. The detector was initially operated at room temperature and the dark current in the detector pixels was useful in distinguishing the boundaries. Next, we cooled the detector and optimized the HV clock delay for cold operations at 183 K. We varied the clock delay value and noted the multiplication gain calculated in the CCCP view application. At the optimal delay for HV clock, the charge shifting in the serial register and the HV register are synchronized leading to optimal multiplication gain. We examined the image and were satisfied with all other parameters for the readout sequence sequence.

The next step in the optimization for the readout sequence was determining the HV

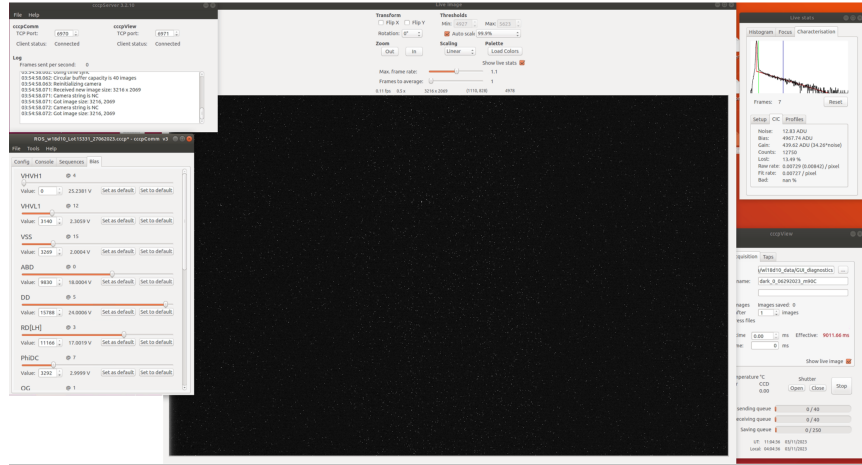


Fig 10: Typical view of GUI during initial testing and optimization of the readout sequence. The HV values were being adjusted using the CCCP Comm (Bottom Left) to get a gain of ~ 1000 e-/e- calculated using the image histogram in the CCCP View (Top right).

values that give similar EM gain at different detector temperatures. At each temperature setting, we varied the HV DAC value in the readout sequence and uploaded it to the controller. We acquired several images at each DAC value to estimate the multiplication gain and find the HV DAC values that gives a multiplication Gain of ~ 1000 e-/e- in the CCCP View GUI. While we will calculate the actual multiplication gain for every image separately using our own reduction script, the multiplication gain estimated in the CCCP view is good for this bench-marking step. The process was repeated for each temperature to create a lookup table for the DAC values for each detector temperature setting. EM gain for each image acuired is estimated durng data reduction, as discussed in section 7.2. A summary of the EM gain measured at each temperature is reported in Table 1.

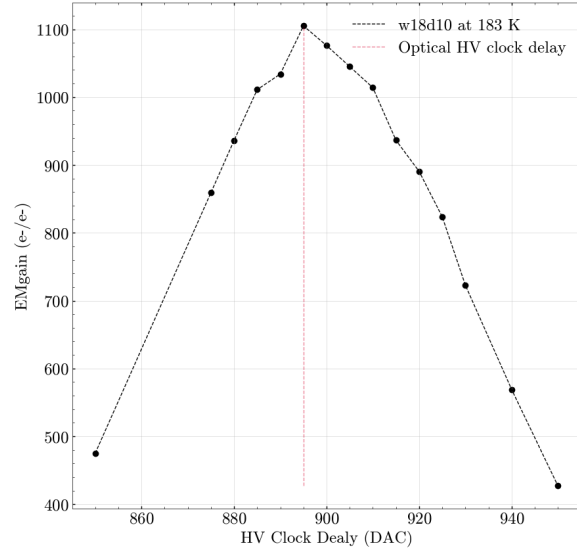


Fig 11: Serial clock delay optimization: Delay of the High voltage serial clock is an important parameter to be optimized in the readout sequence as it is specific to the detector and electronics combination. For this test, we found that a delay DAC value of 895 (corresponding to ~ 925 nanoseconds) maximizes the multiplication gain.

7 Data Acquisition and Data Reduction Pipeline

Introductory paragraph describing next step to previous step. This willr eq

7.1 PTC analysis

The Photon transfer curve data is analyzed using a Python script that first reads the acquisition log to organize the FITS images and creates a database from the metadata. To remove the fixed pattern noise (FPN), consecutive flat images with the same exposure time are subtracted to create a difference-images for each exposure. The script then extracts 13 regions on the detector each to calculate the mean signal and noise in each region for all difference images and store the information for each scan in a database. A sample of PTC

log-log plots between mean signal vs noise is shown in Figure 14. The read noise is estimated by fitting a horizontal line to the low signal part of the curve and the conversion gain is estimated from the x-intercept a line that fits to linear part of the curve.⁴⁷

7.2 Data reduction and photon counting for dark images

The reduction of the dark images taken in PC mode is based on a pipeline developed for noise-characterizing FB2 detectors.²⁰ Figure 12 shows a schematic of the process adopted for the data reduction process in this work. The data for each temperature and VSS combination is reduced independently. The data for each combination is reorganized into image cubes corresponding to each exposure time. The first step is to mask and replace hot pixels, cosmic ray events, and cosmic ray tails and save corrected image cubes. A histogram of corrected images is generated to distinguish read-noise from potential events using appropriate thresholds. However, before the threshold is applied to generate the binary photon counting image, the corrected image cubes are processed with a smearing correction algorithm. A Histogram of each cosmic ray, hot-pixel, and smear-corrected image is used to find the value for 5.5σ threshold to generate a binary image with all pixels above the threshold value identified as events. This threshold image is used to calculate the dark noise, parallel, and serial CIC for each exposure time. The dark noise vs exposure time curve for each combination is used to fit the dark rate. The dark rate is calculated from each combination of d gets the dark rate vs temperature and VSS for the full dataset.

Table 1: Summary of the Temperature and Acquisition Parameters for Dark Measurements. The dark rate was measured at different the detector temperatures with shroud at 298 K and at 230 K. Dark images were acquired with exposure ranging from 0 to 600 seconds. For each detector temperature setting the HV DAC value was set to get a constant EMgain of 1000 e⁻/e⁻. The dark measurements with these settings were repeated for substrate voltage of 0 V, 2 V, and 3 V.

Test ID	Detector Temperature [K]	Shroud Temperature [K]	VSS [V]	Exposure Time Range [s]	HV DAC value	Darks per exposure setting
1	183 ± 0.3	298	0	0-600	8176	5
2	173 ± 0.3	298	0	0-600	7990	5
3	163 ± 0.3	298	0	0-600	7820	5
4	153 ± 0.3	298	0	0-600	7795	5
5	143 ± 0.3	298	0	0-600	7780	5
6	183 ± 0.3	230	0	0-600	8176	5
7	173 ± 0.3	230	0	0-600	7990	5
8	163 ± 0.3	230	0	0-600	7820	5
9	153 ± 0.3	230	0	0-600	7795	5
10	143 ± 0.3	230	0	0-600	7780	5
11	Coming soon: at VSS=2 and VSS=3 for combinations above					

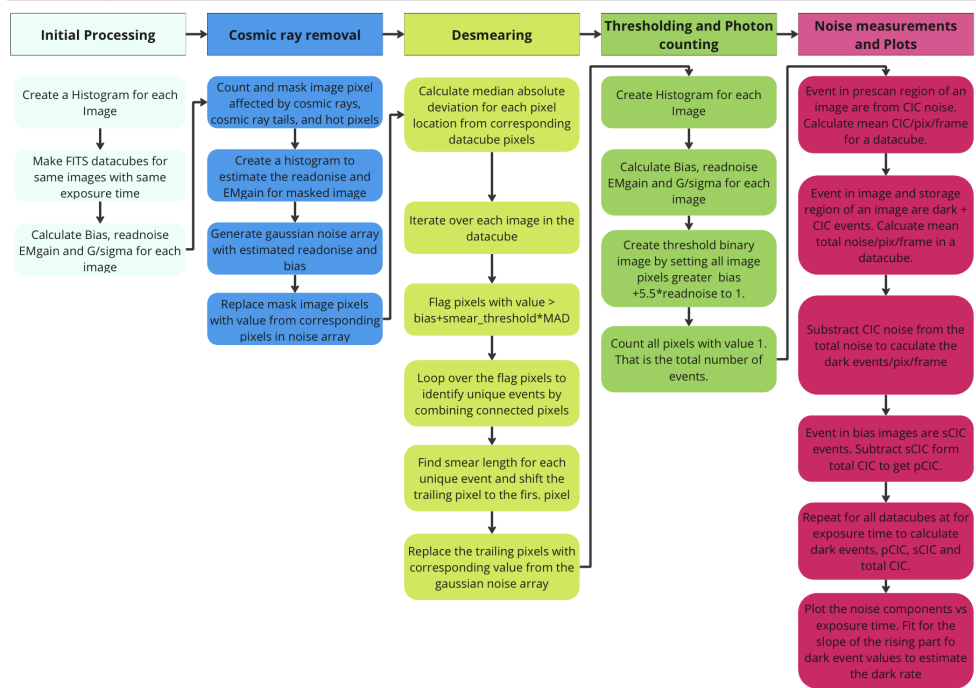


Fig 12: Schematic of dark photon counting data reduction pipeline. Process flow for the analysis of raw dark images acquired from test setup to measure the dark rate. We generate dark rate vs detector temperature for each VSS value at different shroud temperatures.

8 Measurements and Results

In this section, we present our **preliminary results** for read-noise and conversion gain characterisation of our new setup and the first dark measurements with the warm and cold shroud. We took several dataset with the setup to streamline the operations of cooling chains and detector acquisition, optimizing readout sequences, and mitigating light leaks.

8.1 Read noise and conversion gain

We used the Photon Transfer Curve (PTC) technique⁴⁷ to measure the conversion gain and read noise for the detector and the electronics. The data to generate the PTC was taken by uniformly illuminating the detector with a collimated monochromatic beam at 630 nm. Flat-field images were acquired, with the detector temperature 183 K, with progressively increasing exposure times to get different signal levels required to generate the PTC. For each exposure setting, we acquired a dark and a bias image before taking two consecutive flat images followed by a dark and a bias image. For PTC, acquisition, the detectors were operated in conventional mode, i.e. multiplication gain turned off, by lowering the HV clock amplitude to ~ 25 V, to operate the EM register like the serial register of a conventional CCD. The conversion gain and read noise are not affected when the detector is operated in the PC mode.²¹ However, for any changes to the parallel and serial clock parameters would require taking a new PTC data to estimate the read noise and conversion gain, for instance, varying the substrate voltage (VSS).

Figure 13 shows the test setup for the PTC acquisitions (top) and the actual test setup (Left). The Dewar is attached to the collimated output port of our custom Czerny-tuner VUV monochromator based on Mcpherson Model 207V. The setup is windowless so the Monochromator and dewar were pumped down during the acquisitions. The entrance slit is fed by a condenser that focuses light from a deuterium arc lamp. At the exit slit, a pair

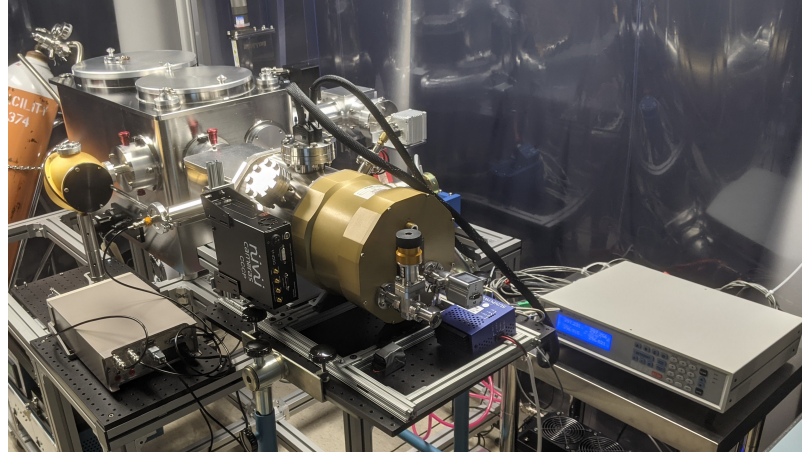


Fig 13: PTC measurements with VUV Monochromator. The detector dewar is attached to the VUV-NIR Monochromator for acquiring sequences of flat images with progressively increasing exposure time generate the PTC. The detector is operated in conventional mode at 183 K.

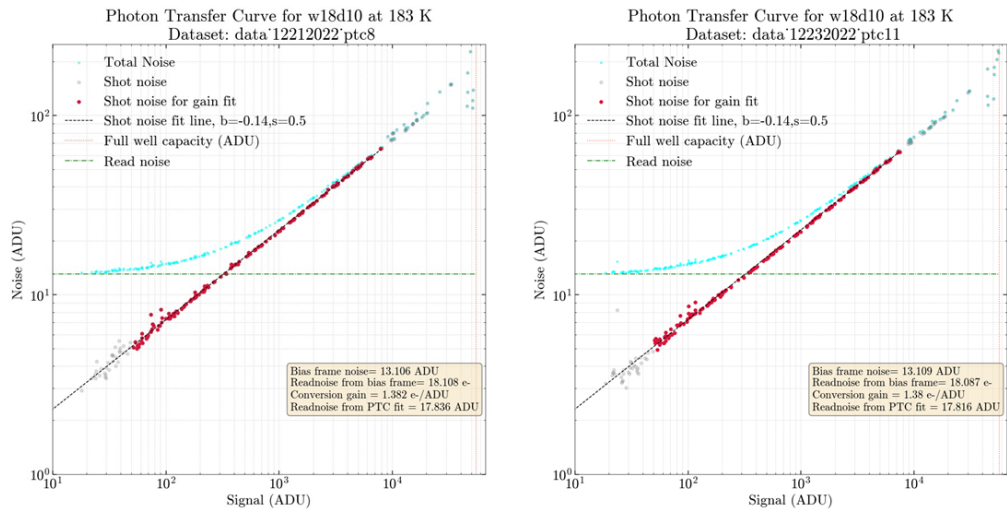


Fig 14: Typical Photon transfer curves. Example of Photon transfer curves for the detector w18d10 in conventional mode at VSS= 0 V. The readnoise is estimated from bias frames and from the fit to the low signal level part of the PTC are in agreement. The conversion gain is obtained by fitting a line to the shot noise-dominated region (red circles) of the curve subtracting the read noise from the total noise.

of collimating optics create a uniform beam that fills the active area of the detector. The exposure is controlled by a shutter, in the monochromator, operated synchronously with the detector exposure sequence through a trigger from the Nüvü controller to the shutter controller. The PTC acquisition is completely automated by a Python application that controls the monochromator operations such as shutter control, wavelength selection, and homing synchronously with the camera operations. For the detector w18d10 used in this study, we found the read noise of $18.1 \text{ e}^- \text{ rms}$ and the conversion gain of $1.38 \text{ e}^-/\text{ADU}$.

8.2 CIC and dark measurements

For each detector temperature and shroud temperature combination listed in Table 1, we took dark exposures while increasing the exposure time between 0 to 600 seconds. Five consecutive dark images followed by five bias exposures were taken for each exposure setting. The multiplication gain was kept at $\sim 1000 \text{ e}^-/\text{e}^-$ by changing the amplitude for the high-voltage clock in the readout sequence for each detector temperature setting. A sample of an unprocessed dark current image is shown in Figure 16. The image has 3216 by 2069 pixels as it includes the prescan, image, and overscan areas. Cosmic ray strikes and trails created by them can also be seen. We reduced the dark images to using the pipeline described in Section 7 to estimate EM gain, Total CIC, Serial CIC, Parallel CIC and dark rate for the combinations of shroud and detector temperatures, and **VSS bias voltages** (Table 2).

Table 2: Sample of the multiplication gain and noise measured in the "Image area" for the tests listed in Table 1. We report the average value of EM gain with 1σ deviation, CIC noise is measured from the bias and prescan data, and the dark rate is estimated by fitting a curve to the image area noise vs exposure time. Comparing the dark rates at the same temperature and similar EM gain indicates that the cold shroud results in lower dark rate.

Test ID	EM gain [e^-/e^-]	Serial CIC [$e^-/\text{pix/frame}$]	Parallel CIC [$e^-/\text{pix/frame}$]	Total CIC [$e^-/\text{pix/frame}$]	Dark Rate [$e^-/\text{pix/hr}$]
1	1095.6 ± 178.7	5.5×10^{-3}	5.3×10^{-3}	1.07×10^{-2}	4.53×10^{-1}
2	1147.3 ± 103.8	4.0×10^{-3}	5.2×10^{-3}	9.0×10^{-3}	6.74×10^{-2}
3	1098.2 ± 131.4	3.7×10^{-3}	4.7×10^{-3}	8.5×10^{-3}	1.36×10^{-2}
4	1059.9 ± 160.2	4.3×10^{-3}	5.9×10^{-3}	1.02×10^{-2}	1.80×10^{-2}
5	1094.6 ± 176.7	4.8×10^{-3}	7.5×10^{-3}	1.22×10^{-2}	2.84×10^{-2}
6	1082.7 ± 173.2	4.8×10^{-3}	5.3×10^{-3}	1.01×10^{-2}	3.46×10^{-1}
7	1090.7 ± 171.5	3.9×10^{-3}	4.9×10^{-3}	8.8×10^{-3}	3.20×10^{-2}
8	1085.5 ± 170.9	3.9×10^{-3}	4.8×10^{-3}	8.7×10^{-3}	< CIC
9	1093.1 ± 170.8	4.4×10^{-3}	6.1×10^{-3}	1.06×10^{-2}	< CIC
10	1088.7 ± 170.7	4.8×10^{-3}	7.5×10^{-3}	1.22×10^{-2}	< CIC

The dark rate vs temperature plot shown in Figure 15, we see the dark current plateau with darks taken with the warm shroud. We also found that the dark rate is lower in darks taken with a cold shroud than the darks taken with a warm shroud. For the cold shroud measurements, the dark rate is not detectable above the CIC noise floor at detector temperatures below 173 K, while it is lower than the warm shroud measurements at 173 K and 183 K. Considering the CIC and EMGain are comparable for two cases, this difference could be attributed to the difference in the surrounding temperature. These results support our hypothesis that the black body radiation from ambient environment has some contribution to the dark rate. However, further investigation is needed to quantify this contribution

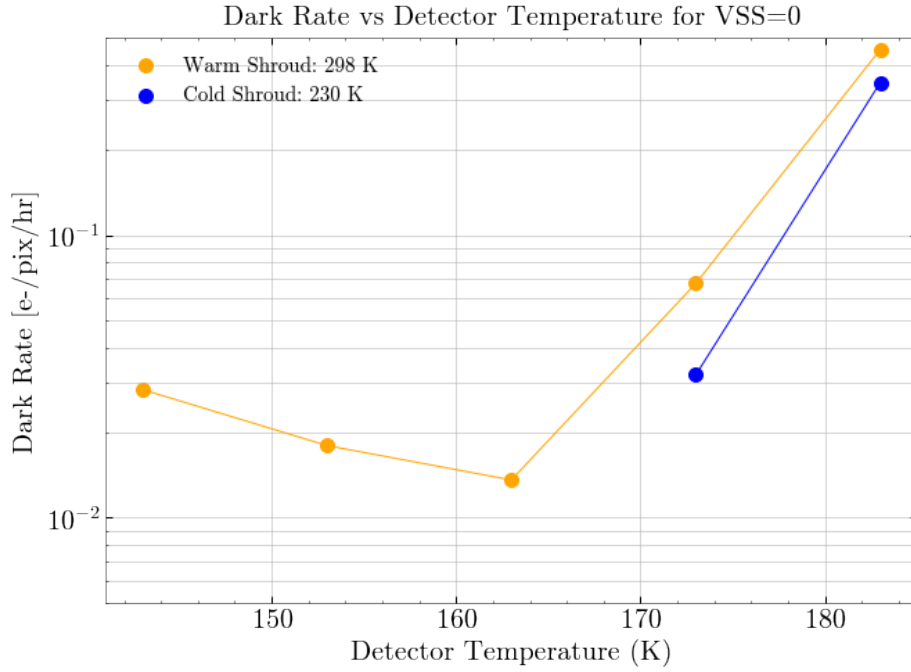


Fig 15: Dark rate vs Detector Temperature with shroud at 298 K (warm) and 230 K (cold) at VSS=0. The dark rates with warm shroud have a plateau similar to Kyne et. al.⁵ The dark rates in cold shroud case are lower than the warm shroud case for the same detector temperature. For temperatures below 173 K dark rates are below detection limit set by the CIC noise floor.

with measurements of dark current with cold shroud at lower detector temperatures. For this we plan to reduce the CIC floor by further optimizing the 1 MHz board or by using a board with the 10 MHz clock which is expected to have lower CIC.

9 Conclusion and Future Work

Our preliminary analysis reproduces the dark plateau that was reported by previous work. We also find that the dark current decreases when the detector is operated in cold shroud with dark rate becoming undetectable at lower detector temperatures. As a part of this

work, we will further investigate this with different VSS voltages and by adding longer dark measurements for the cold shroud runs with this detector. For future work, we will optimize the parallel and serial clocks to reduce the CIC and add more devices.

Additional Figures

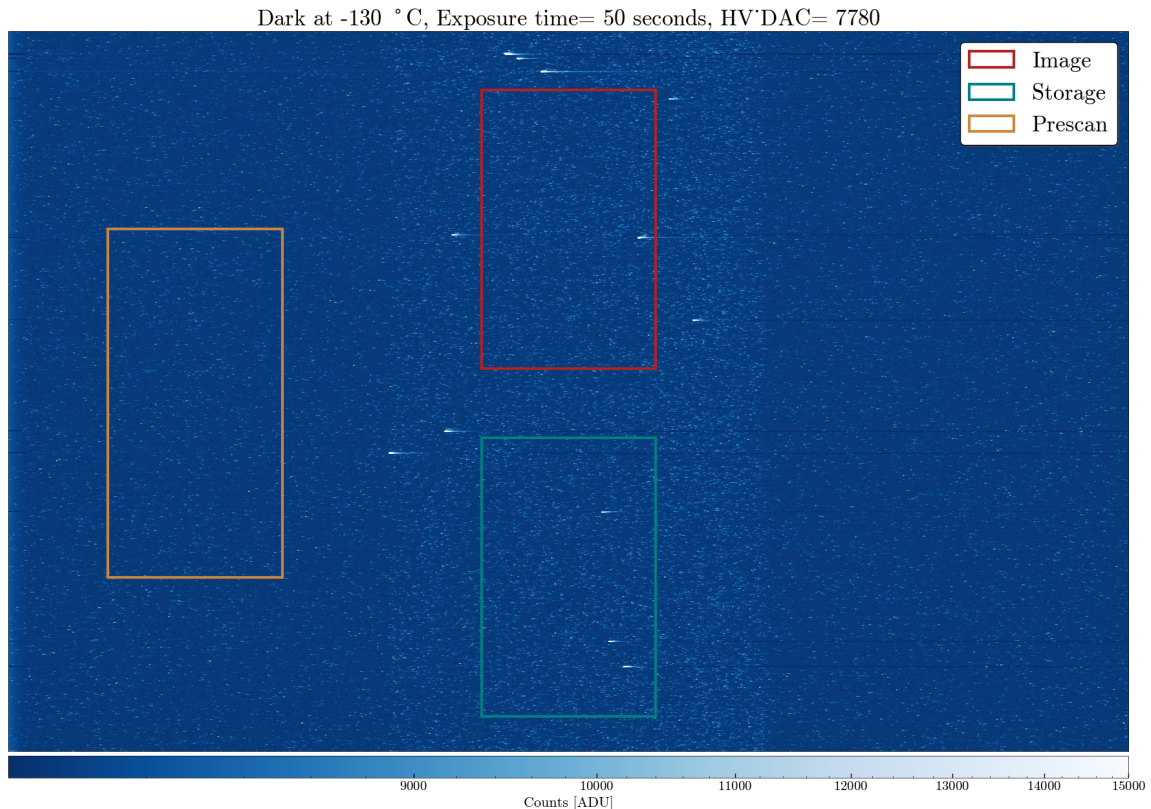


Fig 16: Typical Raw dark Image. Example of a processed raw dark image acquired for this work. The pixels in $\sim 2\text{k}\times 1\text{k}$ area in the middle are the actual detector pixels while the area to the left and the right are the prescan and the overscan. The extraction regions for the image, storage, and prescan area are used for the estimation of noise characteristics and are marked with colored boxes. The storage and image area are analyzed separately for comparison and the prescan region area for estimation of CIC.

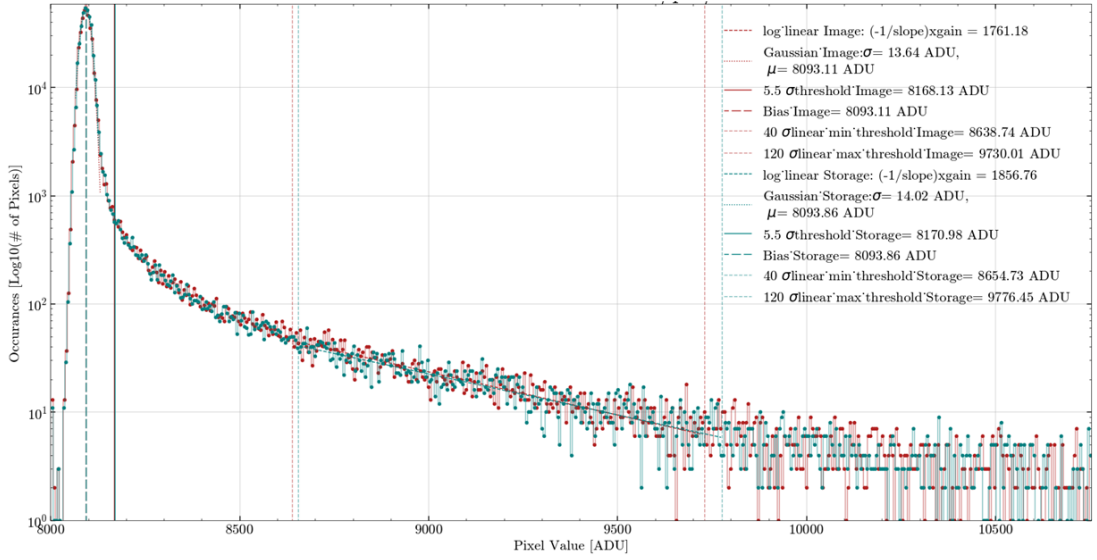


Fig 17: Typical histogram of a 10-second long dark image: Dark image histograms are used to estimate read noise (σ), the threshold value for photon counting, and the multiplication gain. These histograms were generated from the Image and Storage regions of a dark Image taken for this work at 143 K with the 1MHz HV clock and a multiplication gain of 1716 e⁻/e⁻. A Gaussian is fit around the peak of each histogram to estimate the read noise and bias. The multiplication gain is estimated from the inverse of the slope of a line fit to the linear region of the histogram. We set the photon counting threshold to 5.5σ above which a pixel is counted as an event.

References

- 1 M. E. Hoenk, P. J. Grunthaner, F. J. Grunthaner, *et al.*, “Growth of a delta-doped silicon layer by molecular beam epitaxy on a charge-coupled device for reflection-limited ultraviolet quantum efficiency,” *Applied Physics Letters* **61**, 1084–1086 (1992).
- 2 S. Nikzad, M. Hoenk, P. Grunthaner, *et al.*, “Delta-doped ccds: high qe with long-term stability at uv and visible wavelengths,” *Astronomical Telescopes and Instrumentation* (1994).
- 3 S. Nikzad, M. E. Hoenk, F. Greer, *et al.*, “Delta-doped electron-multiplied ccd with absolute quantum efficiency over 50% in the near to far ultraviolet range for single photon counting applications,” *Appl. Opt.* **51**, 365–369 (2012).
- 4 S. Nikzad, A. D. Jewell, M. E. Hoenk, *et al.*, “High-efficiency UV/optical/NIR detectors for large aperture telescopes and UV explorer missions: development of and field observations with delta-doped arrays,” *Journal of Astronomical Telescopes, Instruments, and Systems* **3**(03), 1 (2017).
- 5 G. Kyne, E. T. Hamden, N. Lingner, *et al.*, “The faint intergalactic-medium redshifted emission balloon: future UV observations with EMCCDs,” in *High Energy, Optical, and Infrared Detectors for Astronomy VII*, A. D. Holland and J. Beletic, Eds., **9915**, 61 – 70, International Society for Optics and Photonics, SPIE (2016).

- 6 E. T. Hamden, F. Greer, D. Schiminovich, *et al.*, “UV photon-counting CCD detectors that enable the next generation of UV spectroscopy missions: AR coatings that can achieve 80-90Infrared Detectors for Astronomy V, A. D. Holland and J. W. Beletic, Eds., **8453**, 55 – 61, International Society for Optics and Photonics, SPIE (2012).
- 7 J. Hennessy, A. D. Jewell, M. E. Hoenk, *et al.*, “Materials and process development for the fabrication of far ultraviolet device-integrated filters for visible-blind Si sensors,” in *Image Sensing Technologies: Materials, Devices, Systems, and Applications IV*, N. K. Dhar and A. K. Dutta, Eds., **10209**, 116 – 124, International Society for Optics and Photonics, SPIE (2017).
- 8 J. Hennessy, A. D. Jewell, M. E. Hoenk, *et al.*, “Metal–dielectric filters for solar–blind silicon ultraviolet detectors,” *Appl. Opt.* **54**, 3507–3512 (2015).
- 9 E. Hamden, D. C. Martin, B. Milliard, *et al.*, “FIREBall-2: The faint intergalactic medium redshifted emission balloon telescope,” *The Astrophysical Journal* **898**, 170 (2020).
- 10 J. Gamaunt, L. Jensen, P. Scowen, *et al.*, “Star-Planet Activity Research Cube-Sat (SPARCS): instrument vacuum testing setup,” in *Space Telescopes and Instrumentation 2022: Ultraviolet to Gamma Ray*, J.-W. A. den Herder, S. Nikzad, and

- K. Nakazawa, Eds., **12181**, 121813L, International Society for Optics and Photonics, SPIE (2022).
- 11 E. Hamden, D. Schiminovich, S. Nikzad, *et al.*, “Hyperion: The origin of the stars a far-uv space telescope for high-resolution spectroscopy over wide fields,” (2022).
- 12 H. Chung, “Nox: 12u cubesat mission for characterizing all-sky fuv background.” Talk, Arizona Space Institute Symposium (2022).
- 13 E. Hamden, “Eos, daughter of hyperion.” Talk, Arizona Space Institute Symposium (2022).
- 14 P. Jerram, P. J. Pool, R. Bell, *et al.*, “The LLCCD: low-light imaging without the need for an intensifier,” in *Sensors and Camera Systems for Scientific, Industrial, and Digital Photography Applications II*, N. Sampat, J. Canosa, M. M. Blouke, *et al.*, Eds., **4306**, 178 – 186, International Society for Optics and Photonics, SPIE (2001).
- 15 C. D. Mackay, R. N. Tubbs, R. Bell, *et al.*, “Subelectron read noise at MHz pixel rates,” in *Sensors and Camera Systems for Scientific, Industrial, and Digital Photography Applications II*, N. Sampat, J. Canosa, M. M. Blouke, *et al.*, Eds., **4306**, 289 – 298, International Society for Optics and Photonics, SPIE (2001).
- 16 S. M. Tulloch and V. S. Dhillon, “On the use of electron-multiplying CCDs for astronomical spectroscopy,” *Monthly Notices of the Royal Astronomical Society* **411**, 211–225 (2011).

- 17 P. Morrissey, L. K. Harding, N. L. Bush, *et al.*, “Flight photon counting electron multiplying charge coupled device development for the Roman Space Telescope coronagraph instrument,” *Journal of Astronomical Telescopes, Instruments, and Systems* **9**(1), 016003 (2023).
- 18 J. Hynecek, “Impactron-a new solid state image intensifier,” *IEEE Transactions on Electron Devices* **48**(10), 2238–2241 (2001).
- 19 O. Daigle, J.-L. Gach, C. Guillaume, *et al.*, “CCCP: a CCD controller for counting photons,” in *Ground-based and Airborne Instrumentation for Astronomy II*, I. S. McLean and M. M. Casali, Eds., **7014**, 2288 – 2297, International Society for Optics and Photonics, SPIE (2008).
- 20 G. Kyne, E. T. Hamden, S. Nikzad, *et al.*, “Delta-doped electron-multiplying CCDs for FIREBall-2,” *Journal of Astronomical Telescopes, Instruments, and Systems* **6**(1), 1 – 16 (2020).
- 21 O. Daigle, C. Carignan, J.-L. Gach, *et al.*, “Extreme faint flux imaging with an emccd,” *Publications of the Astronomical Society of the Pacific* **121**, 866 (2009).
- 22 O. Daigle, O. Djazovski, D. Laurin, *et al.*, “Characterization results of EMCCDs for extreme low-light imaging,” in *High Energy, Optical, and Infrared Detectors for Astronomy V*, A. D. Holland and J. W. Beletic, Eds., **8453**, 845303, International Society for Optics and Photonics, SPIE (2012).

- 23 O. Daigle, J. Veilleux, F. J. Grandmont, *et al.*, “Nancy Grace Roman Space Telescope coronagraph EMCCD flight camera electronics development,” in *Space Telescopes and Instrumentation 2022: Optical, Infrared, and Millimeter Wave*, L. E. Coyle, S. Matsuura, and M. D. Perrin, Eds., **12180**, 1218064, International Society for Optics and Photonics, SPIE (2022).
- 24 N. Bush, J. Heymes, D. Hall, *et al.*, “Measurement and optimization of clock-induced charge in electron multiplying charge-coupled devices,” *Journal of Astronomical Telescopes, Instruments, and Systems* **7**(1), 016002 (2021).
- 25 J. Tumlinson, M. S. Peeples, and J. K. Werk, “The circumgalactic medium,” *Annual Review of Astronomy and Astrophysics* **55**, 389–432 (2017).
- 26 J. M. Shull, B. D. Smith, and C. W. Danforth, “THE BARYON CENSUS IN a MULTIPHASE INTERGALACTIC MEDIUM: 30% OF THE BARYONS MAY STILL BE MISSING,” *The Astrophysical Journal* **759**, 23 (2012).
- 27 R. Dave, R. Cen, J. P. Ostriker, *et al.*, “Baryons in the warm hot intergalactic medium,” *The Astrophysical Journal* **552**, 473–483 (2001).
- 28 R. Cen and J. P. Ostriker, “Where are the baryons?,” *The Astrophysical Journal* **514**(1), 1 (1999).
- 29 M. Haider, D. Steinhauser, M. Vogelsberger, *et al.*, “Large-scale mass distribution

- in the Illustris simulation,” *Monthly Notices of the Royal Astronomical Society* **457**, 3024–3035 (2016).
- 30 A. de Graaff, Y.-C. Cai, C. Heymans, *et al.*, “Probing the missing baryons with the sunyaev-zel’dovich effect from filaments,” *Astronomy & Astrophysics* **624**, A48 (2019).
- 31 J. Tumlinson, C. Thom, J. K. Werk, *et al.*, “The large, oxygen-rich halos of star-forming galaxies are a major reservoir of galactic metals,” *Science* **334**, 948–952 (2011).
- 32 S. H. Lim, H. J. Mo, H. Wang, *et al.*, “Detection of missing baryons in galaxy groups with kinetic sunyaev–zel’dovich effect,” *The Astrophysical Journal* **889**, 48 (2020).
- 33 R. A. Crain, V. R. Eke, C. S. Frenk, *et al.*, “The baryon fraction of CDM haloes,” *Monthly Notices of the Royal Astronomical Society* **377**, 41–49 (2007).
- 34 Y. Faerman, A. Sternberg, and C. F. McKee, “Massive warm/hot galaxy coronae as probed by uv/x-ray oxygen absorption and emission. i. basic model,” *The Astrophysical Journal* **835**, 52 (2017).
- 35 J.-T. Li, J. N. Bregman, Q. D. Wang, *et al.*, “Baryon budget of the hot circumgalactic medium of massive spiral galaxies,” *The Astrophysical Journal* **855**, L24 (2018).
- 36 C. Martin, “IGM and CGM emission mapping: A new window on galaxy and structure formation,” *Bulletin of the AAS* **51** (2019). <https://baas.aas.org/pub/2020n3i510>.

- 37 R. Augustin, S. Quiret, B. Milliard, *et al.*, “Emission from the circumgalactic medium: from cosmological zoom-in simulations to multiwavelength observables,” *Monthly Notices of the Royal Astronomical Society* **489**, 2417–2438 (2019).
- 38 C. Martin, S. Nikzad, and D. . Schiminovich, “Next Generation UV Instrument Technologies,” tech. rep., Keck Institute for Space Studies.
- 39 J. C. Green, C. S. Froning, S. Osterman, *et al.*, “THE COSMIC ORIGINS SPEC-TROGRAPH,” *The Astrophysical Journal* **744**, 60 (2011).
- 40 N. R. Council, *New Worlds, New Horizons in Astronomy and Astrophysics*, The National Academies Press, Washington, DC (2010).
- 41 C. Kouveliotou, E. Agol, N. Batalha, *et al.*, “Enduring quests-daring visions (nasa astrophysics in the next three decades),” (2014).
- 42 B. Fleming, M. Quijada, J. Hennessy, *et al.*, “Advanced environmentally resistant lithium fluoride mirror coatings for the next generation of broadband space observatories,” *Appl. Opt.* **56**, 9941–9950 (2017).
- 43 G. Kyne, E. T. Hamden, S. Nikzad, *et al.*, “Delta-doped electron-multiplying CCDs for FIREBall-2,” *Journal of Astronomical Telescopes, Instruments, and Systems* **6**(1), 011007 (2020).
- 44 O. Daigle, P.-O. Quirion, and S. Lessard, “The darkest EMCCD ever,” in *High Energy, Optical, and Infrared Detectors for Astronomy IV*, A. D. Holland and D. A.

Dorn, Eds., **7742**, 774203, International Society for Optics and Photonics, SPIE (2010).

- 45 O. Daigle, J.-L. Gach, C. Guillaume, *et al.*, “CCCP: a CCD controller for counting photons,” in *Ground-based and Airborne Instrumentation for Astronomy II*, I. S. McLean and M. M. Casali, Eds., **7014**, 70146L, International Society for Optics and Photonics, SPIE (2008).
- 46 W. Joye, “SAOImageDS9/SAOImageDS9 v8.0.1.” Zenodo (2019).
- 47 J. R. Janesick, *Scientific Charge-Coupled Devices* (2001).

List of Figures

- 1 Dark current rates as a function of temperature. This plot shows dark current rates for two engineering-grade devices and a delta-doped device with a 10 MHz serial clock. The image area and storage area are plotted for engineering devices. Colors represent different devices and substrate voltages. (Adapted from Kyne 2016⁵)

- 2 Schematic of the test setup, illustrating the vacuum Dewar, detector and detector controller, detector and shroud cooling systems, and ancillary components including the water cooling for the cryocooler, vacuum pump system, automatic LN2 refill system, and Ultra-High Purity Gaseous Nitrogen supply for purging. [Draft Figure]
- 3 Custom Vacuum Dewar setup. CAD representations of vacuum setup depicting the custom extension attached to the ND8 Dewar and the configuration of the cyrocooler, Nüvü CCCP v3 controller, interfaces for the mechanical heat-switch and electrical feed-throughs.
- 4 Detector Cold finger design. CAD view showing the two part copper cold finger. The cold finger 1 (CF1) and cold finger 2 (CF2) are designed to maintain the contact between the back of the detector and the tip of the CF1 from room to cryogenic temperature. An Invar spacer is between the CF1 and CF2 acts like a metering structure while the thermal contact between the two is through two flexible copper straps.
- 5 CAD section of the thermal shroud cooling chain. The shroud surrounding the detector and FEE is cooled through a direct conductive path to the LN2 vessel. A temperature sensor on the shroud is used to control the temperature with patch heaters operated by a closed-loop temperature controller.

- 6 Test flow diagram shows all the tests and validation steps involved in the characterization of the detector CIC and dark noise.
- 7 PCB validation testing: a) Bench test setup for Laboratory detector with the 1 MHz board with the Nüvü controller. Waveforms for High voltage clock (b), one of the four phases of Image clock (c), and one of the serial clocks (d) are shown. These were measured by probing the corresponding pins on the ZIF socket of the 1 MHz board. The HV and the image clocks have a sinusoidal profile while the serial clocks have arbitrary shapes.
- 8 Images showing the different components of the test setup. a) Vacuum Dewar with the turbo pump The custom Samtech flange and the flange for thermal sensor and heater wiring, b) Mechanical detector package with the temperature sensor bonded on the surface of the sensor, c) Internal view of the Dewar showing the vacuum shroud and the Samtech cable. d) Experimental setup, consisting of Dewar, detector controller, the LN2 cooling system, temperature controller, and vacuum pump.
- 9 Sample of the temperature profile for cooling the detector. The cryocooler is intermittently shut to keep the CF1 in contact with the detector back-plane and to keep the detector cooling rate of the detector well within 5K/min limit.

- 10 Typical view of GUI during initial testing and optimization of the readout sequence. The HV values were being adjusted using the CCCP Comm (Bottom Left) to get a gain of ~ 1000 e-/e- calculated using the image histogram in the CCCP View (Top right).
- 11 Serial clock delay optimization: Delay of the High voltage serial clock is an important parameter to be optimized in the readout sequence as it is specific to the detector and electronics combination. For this test, we found that a delay DAC value of 895 (corresponding to ~ 925 nanoseconds) maximizes the multiplication gain.
- 12 Schematic of dark photon counting data reduction pipeline. Process flow for the analysis of raw dark images acquired from test setup to measure the dark rate. We generate dark rate vs detector temperature for each VSS value at different shroud temperatures.
- 13 PTC measurements with VUV Monochromator. The detector dewar is attached to the to VUV-NIR Monochromator for acquiring sequences of flat images with progressively increasing exposure time generate the PTC. The detector is operated in conventional mode at 183 K.

- 14 Typical Photon transfer curves. Example of Photon transfer curves for the detector w18d10 in conventional mode at VSS= 0 V. The readnoise is estimated from bias frames and from the fit to the low signal level part of the PTC are in agreement. The conversion gain is obtained by fitting a line to the shot noise-dominated region (red circles) of the curve subtracting the read noise from the total noise.
- 15 Dark rate vs Detector Temperature with shroud at 298 K (warm) and 230 K (cold) at VSS=0. The dark rates with warm shroud have a plateau similar to Kyne et. al.⁵ The dark rates in cold shroud case are lower than the warm shroud case for the same detector temperature. For temperatures below 173 K dark rates are below detection limit set by the CIC noise floor.
- 16 Typical Raw dark Image. Example of a processed raw dark image acquired for this work. The pixels in $\sim 2\text{k}\times 1\text{k}$ area in the middle are the actual detector pixels while the area to the left and the right are the prescan and the overscan. The extraction regions for the image, storage, and prescan area are used for the estimation of noise characteristics and are marked with colored boxes. The storage and image area are analyzed separately for comparison and the prescan region area for estimation of CIC.

17 Typical histogram of a 10-second long dark image: Dark image histograms are used to estimate read noise (σ), the threshold value for photon counting, and the multiplication gain. These histograms were generated from the Image and Storage regions of a dark Image taken for this work at 143 K with the 1MHz HV clock and a multiplication gain of 1716 e⁻/e⁻. A Gaussian is fit around the peak of each histogram to estimate the read noise and bias. The multiplication gain is estimated from the inverse of the slope of a line fit to the linear region of the histogram. We set the photon counting threshold to 5.5σ above which a pixel is counted as an event.

List of Tables

1 Summary of the Temperature and Acquisition Parameters for Dark Measurements. The dark rate was measured at different the detector temperatures with shroud at 298 K and at 230 K. Dark images were acquired with exposure ranging from 0 to 600 seconds. For each detector temperature setting the HV DAC value was set to get a constant EMgain of 1000 e⁻/e⁻. The dark measurements with these settings were repeated for substrate voltage of 0 V, 2 V, and 3 V.

2 Sample of the multiplication gain and noise measured in the "Image area" for the tests listed in Table 1. We report the average value of EM gain with 1σ deviation, CIC noise is measured from the bias and prescan data, and the dark rate is estimated by fitting a curve to the image area noise vs exposure time. Comparing the dark rates at the same temperature and similar EM gain indicates that the cold shroud results in lower dark rate.